EES Batteries

ROYAL SOCIETY OF CHEMISTRY

PAPER

View Article Online
View Journal | View Issue

Cite this: *EES Batteries*, 2025, **1**, 609

Achieving high capacity and long cycling life in aqueous zinc–sulfur batteries with improved kinetics through electrolyte solvation engineering†

Tino S. Thomas, Aayushi Prakash Sinha and Debaprasad Mandal *

Aqueous Zn/S batteries are emerging as promising next-generation high-energy density rechargeable storage devices. The cost-effective and abundant reserve of sulfur, when paired with a zinc anode, significantly enhances both specific capacity and energy density. However, their practical applications face challenges such as poor sulfur utilization in aqueous electrolytes, sluggish sulfur redox kinetics and parasitic reactions at the Zn anode. To address these challenges, electrolyte engineering strategies have been introduced using high donor number (DN) organic co-solvents. Extensive investigation into the impact of DN on sulfur conversion kinetics and the Zn anode reveals that DMSO, a high-DN solvent, facilitates efficient reversibility of sulfur and prevents the hydrogen evolution reaction (HER) and dendrite formation on the zinc anode by modulating the solvation sheath of Zn^{2+} ions. Notably, the high DN of DMSO enables a lower concentration of additives while improving the kinetics of both the sulfur cathode and the zinc anode, compared to higher concentrations of low-DN solvents like acetonitrile and DMF. As a result, the Zn/S battery with a DMSO-containing electrolyte achieved a high specific capacity of 1502 mA h g^{-1} at 0.1 A g^{-1} and long-term cycling stability with 92% capacity retention over 1000 cycles at 5 A g^{-1}.

Received 31st March 2025,
Accepted 16th April 2025

DOI: 10.1039/d5eb00063g

rsc.li/EESBatteries

Broader context

Aqueous Zn/S batteries offer significant advantages, including the impressive theoretical specific capacity and abundant natural reserves of sulfur and cost-effective zinc as an anode. However, their practical application is hindered by issues such as corrosion, the hydrogen evolution reaction (HER), dendrite formation at the Zn anode, and poor utilization of the sulfur cathode due to solid–solid conversion. Addressing these issues at both the Zn anode and the S cathode is crucial for the development of high-performance Zn/S batteries. Our study demonstrates the pivotal role of the donor number of organic co-solvents as additives in mitigating these challenges. High-DN solvents promote uniform Zn stripping/plating and minimize the HER by modulating the Zn^{2+} ion solvation sheath. Furthermore, high-DN solvents aid in enhancing sulfur utilization and reversibility, resulting in high energy-dense Zn/S batteries. As a result, the designed hybrid electrolyte showed cycling stability with 92% capacity retention over 1000 cycles. The advancements in the use of high-DN solvents could lead to the adoption of a cost-effective approach for the rational design of hybrid electrolytes in high-performance aqueous batteries.

1 Introduction

Electrified mobility is rapidly transforming a broad spectrum of the automobile sector, with advancements in energy storage technologies at the forefront. At the core of this revolution lies the advancement of Li-ion batteries (LIBs), which have become a key enabler in driving a shift from a carbon-based to a carbon-neutral society.[1–3] While this progress is remarkable, LIBs are hindered by several limitations, including the geographically constrained availability of lithium, low specific capacity (<400 mA h g^{-1}), and the use of flammable organic electrolytes, which collectively contribute to high production costs and safety concerns.[4] In this regard, Li–S batteries have emerged as a promising alternative, leveraging sulfur as a cathode material due to its high theoretical capacity, abundant reserves, non-toxicity, and cost-effectiveness.[5,6] Despite these advantages, Li–S batteries encounter significant challenges, including the dissolution of lithium polysulfides and their notorious shuttle effect, which result in the loss of active material and rapid capacity fading.[7]

In recent years, aqueous zinc–sulfur (Zn/S) batteries have garnered significant attention due to their combination of the advantages of zinc as an anode and sulfur as a cathode. Zn as an anode offers numerous advantages, such as high theoretical capacity (820 mA h g^{-1}), low redox potential (−0.76 V *vs.* SHE), abundant natural reserves, low toxicity, minimal hydrogen evolution, and excellent compatibility with aqueous

Department of Chemistry, Indian Institute of Technology Ropar, Punjab 140001, India. E-mail: dmandal@iitrpr.ac.in

† Electronic supplementary information (ESI) available. See DOI: https://doi.org/10.1039/d5eb00063g

electrolytes.[8,9] Sulfur, on the other hand, provides a high theoretical capacity of 1675 mA h g^{-1}, non-toxicity, cost-effectiveness, and abundant reserves.[10] Furthermore, aqueous Zn/S batteries operate within the electrochemical stability window of water, leveraging a theoretical voltage of 1.01 V derived from the conversion of sulfur and ZnS. Moreover, the solid–solid conversion of S_8 to ZnS minimizes the polysulfide shuttling seen in other sulfur-based systems.[11,12] Thus, the advancement of aqueous Zn/S batteries has the potential to revolutionize the landscape of aqueous rechargeable energy storage systems, offering a transformative solution for next-generation energy storage technologies.

Despite their potential, the commercialization of aqueous Zn/S batteries faces significant challenges. The solid–solid conversion of sulfur to ZnS suffers from sluggish reaction kinetics, leading to poor energy efficiency and limited cycling stability.[13] Furthermore, the poor wettability of sulfur in aqueous electrolytes hinders zinc-ion mobility at the cathode/electrolyte interface, aggravating polarization and limiting battery performance. On the anode side, Zn is prone to dendritic growth and the hydrogen evolution reaction (HER), leading to reduced cycle life.[14,15] Strategies like electrolyte engineering, sulfur cathode modifications, and Zn anode treatments are critical for addressing these issues.

The incorporation of redox mediators, such as iodine species (I_2/I_3^-), has proven to be an effective strategy for improving the reversibility and reaction kinetics of sulfur cathodes in aqueous Zn/S batteries but greatly accelerates zinc anode corrosion, resulting in rapid battery degradation.[14,16] Additionally, the zinc anodes face fundamental challenges associated with the HER. The high desolvation energy required to strip water molecules from the $[Zn(H_2O)_6]^{2+}$ hydration shell exacerbates the HER, locally generating hydroxide ions (OH^-) that react with zinc to form an insulating $Zn(OH)_2$ layer.[17,18] This passivation layer severely impedes zinc utilization and overall battery efficiency as given below:[12,19]

$$Zn \rightarrow Zn^{2+} + 2e^- \quad (1)$$

$$2H_2O + 2e^- \rightarrow H_2 \uparrow + 2OH^- \quad (2)$$

$$2OH^- + Zn^{2+} \rightarrow Zn(OH)_2 \downarrow \quad (3)$$

To address these challenges, various strategies, such as electrolyte engineering and cathode modification, have been explored, among which the use of organic co-solvents emerges as a promising approach.[11,13,20–29] Organic solvents with high Gutmann donor numbers (DNs) can significantly improve the performance of zinc batteries by modulating the solvation environment.[30] The DN of a solvent quantifies its electron-donating ability, which influences the solubility of reaction intermediates, altering the hydrogen-bonding network in aqueous electrolytes.[31,32] High-DN solvents, particularly polar aprotic solvents, can effectively modify the Zn^{2+} ion solvation structure by disrupting the hydrogen-bonding network of the solvation shell sheath of water as well as replacing water molecules from the coordination sphere.[33–35] This leads to the stabilization of the zinc anode, reduces corrosion, and promotes uniform zinc deposition. Conversely, low-DN solvents fail to adequately manipulate the anode/electrolyte interfacial structure, highlighting the critical role of the DN in tailoring electrolyte properties.[36] High-DN solvents are also known to enhance sulfur kinetics at the cathode in non-aqueous multivalent metal–sulfur batteries, wherein high-DN solvents, owing to their stronger interaction with metal ions, can shield the charge density of the cation, leading to the stability of soft polysulfides.[37,38] Similarly, in the Zn/S system, we hypothesize that high-DN solvents could enable the controlled growth of ZnS discharge products, minimizing passivation and maintaining cathode conductivity during cycling, thus ensuring prolonged cycle life.

This work investigates common cost-effective organic co-solvents that are compatible with aqueous electrolytes bearing different DN values—acetonitrile (ACN, DN = 14.1), dimethylformamide (DMF, DN = 26.6), and dimethyl sulfoxide (DMSO, DN = 29.8)—to stabilize the Zn anode and enhance sulfur kinetics in aqueous electrolytes (Fig. 1). The hybrid electrolytes consist of 2M $Zn(OTf)_2$ and ZnI_2 as the redox mediators. The role of co-solvents with low, moderate, and high DN values is systematically investigated. DMSO demonstrates superior performance, which expands the electrolyte's electrochemical stability window, suppressing the HER, leading to effective inhibition of dendritic growth on the zinc anode and enhancing sulfur redox kinetics. These transformative roles of high-DN organic co-solvent DMSO enable the battery to deliver a high capacity of 1502 mA h g^{-1} at 0.1 A g^{-1} and maintain an excellent capacity retention of 92% for 1000 cycles at a high current density of 5 A g^{-1}.

2 Results and discussion

Electron-donating ability, evaluated by the Gutmann donor number (DN), is pivotal in assessing the role of the electrolyte additive in modulating the solvation sheath, wherein organic molecules with high DNs can replace water molecules from the solvation sheath of zinc ions. This disrupts the original hydrogen-bonding network, leading to a water-deficient solvation structure, and minimizes parasitic reactions such as the HER. Furthermore, the solvation sheath formed by high-DN organic solvents can allow uniform zinc plating, leading to minimized dendritic formation. High-DN solvents can also improve the sulfur kinetics during cycling, resulting in stabilized battery performance.

2.1 Tuning of the solvation shell using co-solvent additives in regulating the Zn^{2+} solvation sheath

To systematically investigate the role of organic co-solvent additives in regulating the Zn^{2+} solvation sheath, three co-solvents with varying donor numbers—ACN, DMF, and DMSO—were taken as the model. FT-IR, ^1H, and ^{19}F NMR spectra of varying ratios of ACN, DMF, and DMSO additives in the presence of aqueous 2 M $Zn(OTf)_2$ were recorded to analyze the interactions between water molecules, co-solvents, and salt.

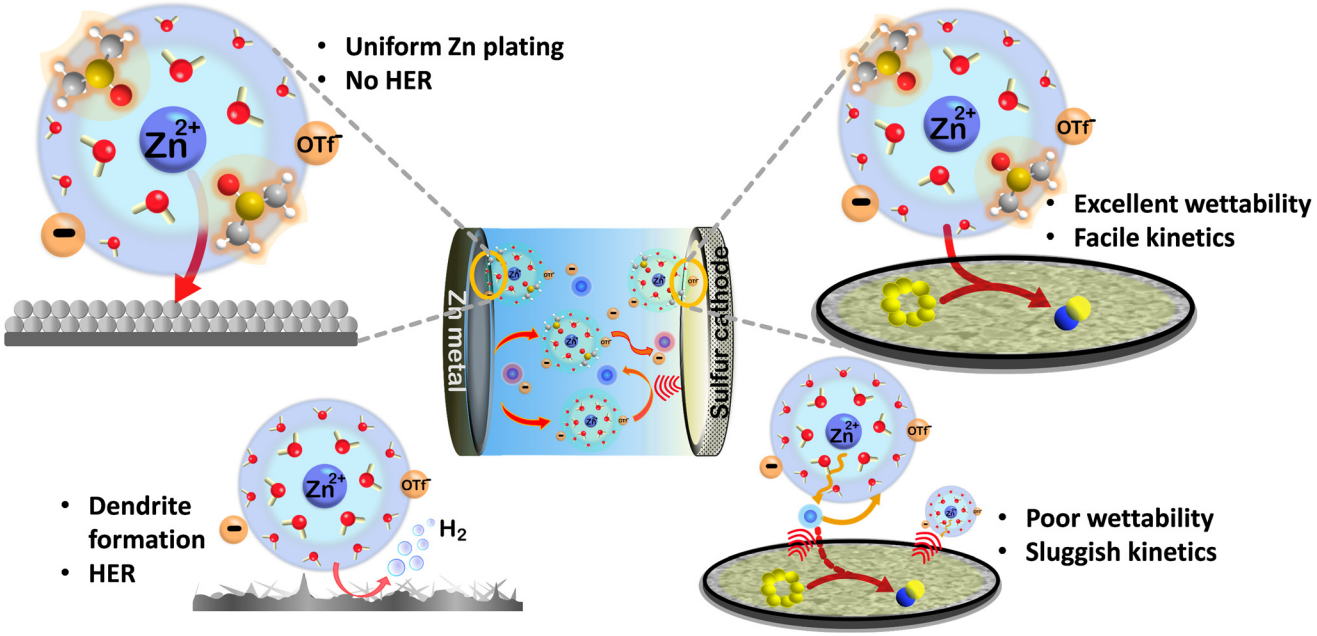

Fig. 1 Schematic representation of the designed hybrid electrolyte for Zn/S batteries.

Initially, FT-IR spectra of aqueous $Zn(OTf)_2$ solution containing 20% v/v of each co-solvent were recorded. The O–H band at 2800–3700 cm^{-1} can be divided into three regions, *viz.*, network water (NW), intermediate water (IW), and multimer water (MW) (Fig. 2a).[39] The reduced intensity of the network water (NW) suggests that co-solvent additives disrupt the hydrogen-bonding network of water molecules. The most significant shift was observed in the case of DMSO-20, highlighting its stronger ability to modulate the solvation structure (Fig. S1a–c, ESI†). The S=O symmetric stretching peak of the OTf anion at 1030 cm^{-1} also showed a slight shift with DMSO addition, confirming the interaction (Fig. 2b). A slight red shift in the S=O stretching peak of DMSO to 1008 cm^{-1} was observed upon addition of $Zn(OTf)_2$, which further demonstrated the modulation of the solvation structure of Zn^{2+} ions by DMSO. Additionally, the broad peak intensified and apparently blue-shifted with increasing DMSO content, arising from intermolecular interactions between DMSO and water (Fig. S1e

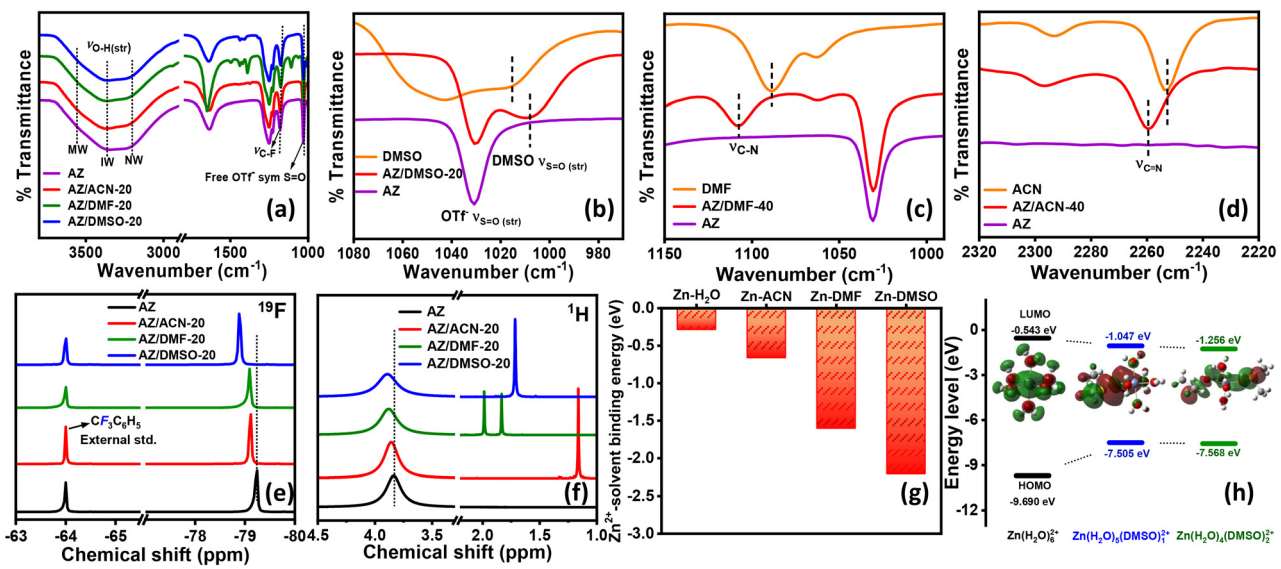

Fig. 2 (a) FT-IR spectra of electrolytes containing additives; FT-IR spectra of (b) DMSO, (c) DMF, and (d) ACN additives; (e) ^{19}F-NMR spectra of electrolytes using trifluorotoluene as an external standard and (f) ^{1}H-NMR spectra of electrolytes using acetone-d_6 as an external standard; (g) binding energy of the solvent–Zn^{2+} complex; and (h) HOMO and LUMO energy levels for different contents of DMSO additives (inset: corresponding LUMO overlap).

and f, ESI†).[40] Similar trends were also observed with the C–F vibration at 1177 cm^{-1} and the shoulder in the broad asymmetric S=O vibration peak of OTf– at 1281 cm^{-1}. This highlights that the presence of DMSO can modulate the coordination structure of both Zn^{2+} and OTf–. Comparable modulation of the solvation shell of the Zn^{2+} ion using DMF and ACN was also observed from their FT-IR spectra. The C=O stretching in DMF shifted to a lower wavenumber when added to water. At the same time, the C–N vibration at 1090 cm^{-1} in DMF is blue-shifted upon Zn salt addition, indicating a similar solvation shell modification, as seen in Fig. 2c, S1h, and i (ESI†). Similarly, in acetonitrile, the C≡N at 2253 cm^{-1} blue-shifted, signifying the solvation shell modulation (Fig. 2d, S1k and l, ESI†).

These findings were corroborated by ^{19}F and ^{1}H NMR analyses of the electrolytes. The ^{19}F-NMR revealed that CF_3 of OTf^- in DMSO (−78.88 ppm) exhibits the maximum downfield shift compared to those of water (−79.27 ppm), ACN (−79.11 ppm), and DMF (−79.08 ppm), owing to its ability to effectively stabilize the Zn^{2+} ion and OTf^- anion, resulting in an increased electron density on the anion (Fig. 2e). Similarly, in ^{1}H NMR, the peak for H_2O shifted downfield from 3.83 ppm to 3.89 ppm, 3.88 ppm, and 3.85 ppm for DMSO-20, DMF-20, and ACN-20, respectively, indicating effective solvent–H_2O interaction (Fig. 2f). These results were further validated by DFT calculations, confirming that DMSO exhibits superior solvation modulation of Zn^{2+} ions.

The donor number (DN) values of these solvents, presented in Fig. S2a (ESI†), serve as a reference point for their zinc-ion coordination capabilities. Density functional theory (DFT) calculations were performed to validate the predicted influence of the DN on solvent affinity towards Zn ions and their coordination efficiency. Zn^{2+}–solvent binding energies were calculated to quantify the interaction strength between Zn^{2+} ions and the co-solvents. As shown in Fig. 2g and S2c (ESI†), DMSO exhibited the lowest binding energy (−2.21 eV) compared to DMF (−1.60 eV), ACN (−0.66 eV), and water (−0.28 eV), indicating its superior coordination affinity with Zn^{2+} ions. Additionally, upon the replacement of water molecules with DMSO in the primary solvation shell of the Zn^{2+} aqua-complex, the LUMO energy level as well as the band gap decreased from 9.14 eV for $[Zn(H_2O)_6]^{2+}$ to 6.45 eV and 6.31 eV for $[Zn(H_2O)_5(DMSO)_1]^{2+}$ and $[Zn(H_2O)_4(DMSO)_2]^{2+}$, respectively, suggesting facile electron donation/acceptance from the Zn anode, as shown in Fig. 2h. This indicates that Zn ions would preferentially interact with DMSO, facilitating more uniform zinc deposition during cycling. These results support the relationship between the DN and the Zn^{2+} ion coordination efficiency, demonstrating that DMSO with a high DN effectively minimizes solvation-related inefficiencies and could promote stable battery performance.

2.2 Electrochemical analysis for optimizing electrolyte performance

To evaluate the effectiveness of co-solvents in minimizing the HER, linear sweep voltammetry (LSV) was conducted using a three-electrode system comprising carbon paper as the inert working electrode, Ag/AgCl/3 M KCl as the reference electrode, and Pt wire as the counter electrode. The experiments were conducted using 2 M $Zn(OTf)_2$ (referred to as AZ) as the electrolytic medium, with varying concentrations of ACN, DMF, and DMSO. As shown in Fig. 3a, electrolytes containing ACN displayed an increase in HER overpotential from −0.99 V to −1.02 V for ACN-20. However, a higher ACN concentration of 60% was needed to substantially suppress the HER. For DMF, a 40% concentration (DMF-40) led to a notable increase in HER overpotential from −0.99 V to −1.10 V (Fig. 3b). In contrast, DMSO-20 effectively suppressed the HER with an overpotential of −1.09 V, which further increased to −1.27 V for DMSO-40 (Fig. 3c). This demonstrates that a lower DMSO concentration is more effective in mitigating the HER than ACN-60 and DMF-40. The HER overpotentials for various co-solvents are listed in Tables S1–S3 (ESI†). The findings were further validated by performing electrochemical impedance spectroscopy (EIS) for various electrolytes to examine the effectiveness of the co-solvents in reducing the HER, as shown in Fig. 3d–f. Increasing the concentration of ACN increased the charge transfer resistance (R_{ct}), reaching a peak value of 15.6 Ω cm^2 for ACN-60. Similarly, the R_{ct} value for DMF increased with increasing DMF concentration, with DMF-40 yielding the highest R_{ct} value. Notably, DMSO-20 outperformed both, showing significantly higher R_{ct} at lower content, effectively minimizing the HER and enhancing the overpotential. However, a higher R_{ct} value would induce sluggish zinc ion adsorption, necessitating a balance. Furthermore, solution resistance (R_s), which provides information about the ionic conductivity for all the systems, was determined from EIS fitting (detailed in Tables S4–S6, ESI†), wherein optimal ratios of ACN/water 60 : 40 v/v, DMF/water 40 : 60 v/v, and DMSO/water 20 : 80 v/v were chosen for subsequent studies. However, to maintain the concentration of organic cosolvents below 50%, ACN 40 : 60 v/v was used. The usage of organic solvents as electrolytes presents significant challenges regarding flammability and safety. To examine the safety benefits of the hybrid electrolyte, the flammability of ACN, DMF, and DMSO as cosolvents was tested. As illustrated in Fig. S3 (ESI†), a separator soaked in pure ACN, DMF, and DMSO ignited instantly upon exposure to flame, whereas the separator immersed in the hybrid electrolytes, AZ/ACN-40/ZnI_2, AZ/DMF-40/ZnI_2, and AZ/DMSO-20/ZnI_2, exhibited nonflammability, underscoring their good safety profile.

This suggests that DMSO, with its higher donor number, is more effective at modulating the solvation shell even at lower concentrations, surpassing ACN and DMF. This highlights its potential as a co-solvent additive for enhancing electrochemical performance in battery systems.

2.3 Corrosion analysis of hybrid electrolytes on the Zn anode

The effectiveness of hybrid electrolytes in mitigating corrosion and minimizing the HER at the Zn anode was assessed using potentiodynamic linear polarization (LP) measurements. A three-electrode setup was employed, with Zn foil, Ag/AgCl/3 M

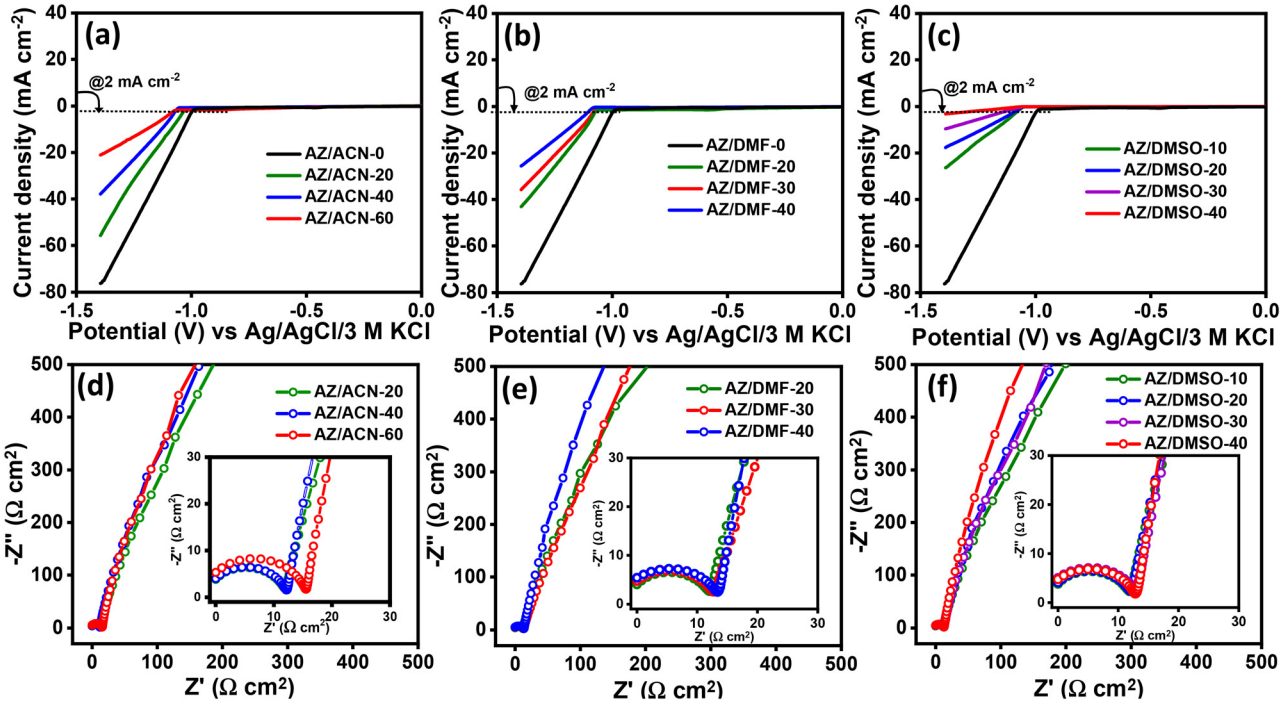

Fig. 3 LSV of (a) ACN; (b) DMF; (c) DMSO-containing electrolytes at a scan rate of 50 mV s^{-1}; EIS spectra of (d) ACN; (e) DMF; (f) DMSO-containing electrolytes using carbon paper as the working electrode, Ag/AgCl/3 M KCl as the reference electrode, and Pt wire as the counter electrode.

KCl, and Pt wire serving as the working, reference, and counter electrodes, respectively. Corrosion studies were performed with electrolytes containing 2 M $Zn(OTf)_2$ (AZ) and 0.05 M ZnI_2 as a redox mediator, including AZ, AZ/ZnI_2, AZ/ACN/ZnI_2, AZ/DMF/ZnI_2, and AZ/DMSO/ZnI_2. The cathodic current, corresponding to the HER, and the anodic current, indicative of zinc-ion mobility, were carefully analyzed to elucidate the role of additives in corrosion inhibition.

The addition of ZnI_2 to AZ (AZ/ZnI_2) leads to an increase in cathodic current, indicating accelerated corrosion of the zinc anode due to zinc iodide. Conversely, hybrid electrolytes AZ/ACN/ZnI_2, AZ/DMF/ZnI_2, and AZ/DMSO/ZnI_2 exhibited reduced corrosion current densities (I_{corr}), demonstrating suppressed corrosion (Fig. S4a–c and Tables S7–S9, ESI†). Among these, the DMSO-based electrolyte showed the most significant effect, with a five-fold decrease in the cathodic current, reducing I_{corr} from 12.6 mA cm^{-2} (AZ/ZnI_2) to 2.6 mA cm^{-2} for AZ/DMSO/ZnI_2. Consequently, the corrosion rate dropped from 371.8 mm y^{-1} to 60.1 mm y^{-1}. Additionally, a negative potential shift was observed, reflecting effective HER suppression (Fig. S4c, ESI†).

EIS further corroborated these findings, showing a higher R_{ct} value in the hybrid electrolytes, with the DMSO-based electrolyte exhibiting the highest R_{ct} value compared to AZ/ZnI_2 (Fig. S4d–f†). Collectively, the AZ/DMSO/ZnI_2 hybrid electrolyte effectively suppressed the HER, minimized zinc corrosion, and maintained Zn ion mobility, highlighting its potential to enhance battery performance.

2.4 Full-cell performance evaluation of Zn/S batteries

Full-cell Zn/S batteries were assembled using the S@AC cathode with Zn foil as the anode and various electrolytes. To address the inherently poor conductivity of sulfur, activated carbon was incorporated *via* melt diffusion to yield S@AC (detailed in the ESI†). The successful infusion of sulfur into the carbon matrix was confirmed by powder X-ray diffraction (PXRD), where the loss of long-range ordered sulfur peaks indicates effective incorporation (Fig. S5a, ESI†). X-ray photoelectron spectroscopy (XPS) of the S@AC composite further validated the presence of elemental sulfur in the carbon matrix through the peaks at 164.2 eV and 165.3 eV corresponding to $S2p_{3/2}$ and $S2p_{1/2}$, respectively (Fig. S5b, ESI†). Thermogravimetric analysis (TGA) confirmed 51 wt% sulfur content in S@AC (Fig. S5c, ESI†).[12] Additionally, FESEM images revealed the morphological and microstructural characteristics of both AC and S@AC, highlighting a uniform distribution of carbon and sulfur, as evidenced by elemental dot mapping of S@AC (Fig. S5d–g, ESI†).

Using the S@AC cathode, full-cell Zn/S batteries were assembled with Zn foil as the anode and electrolytes composed of 2 M $Zn(OTf)_2$ and 0.05 M ZnI_2 in water, ACN-40, DMF-40, and DMSO-20 solvents. The electrochemical performance was evaluated through galvanostatic charge–discharge (GCD) and cyclic voltammetry (CV) tests. Fig. 4a demonstrates the charge–discharge behaviour of Zn/S batteries in three hybrid electrolytes. The discharge voltage notably increases

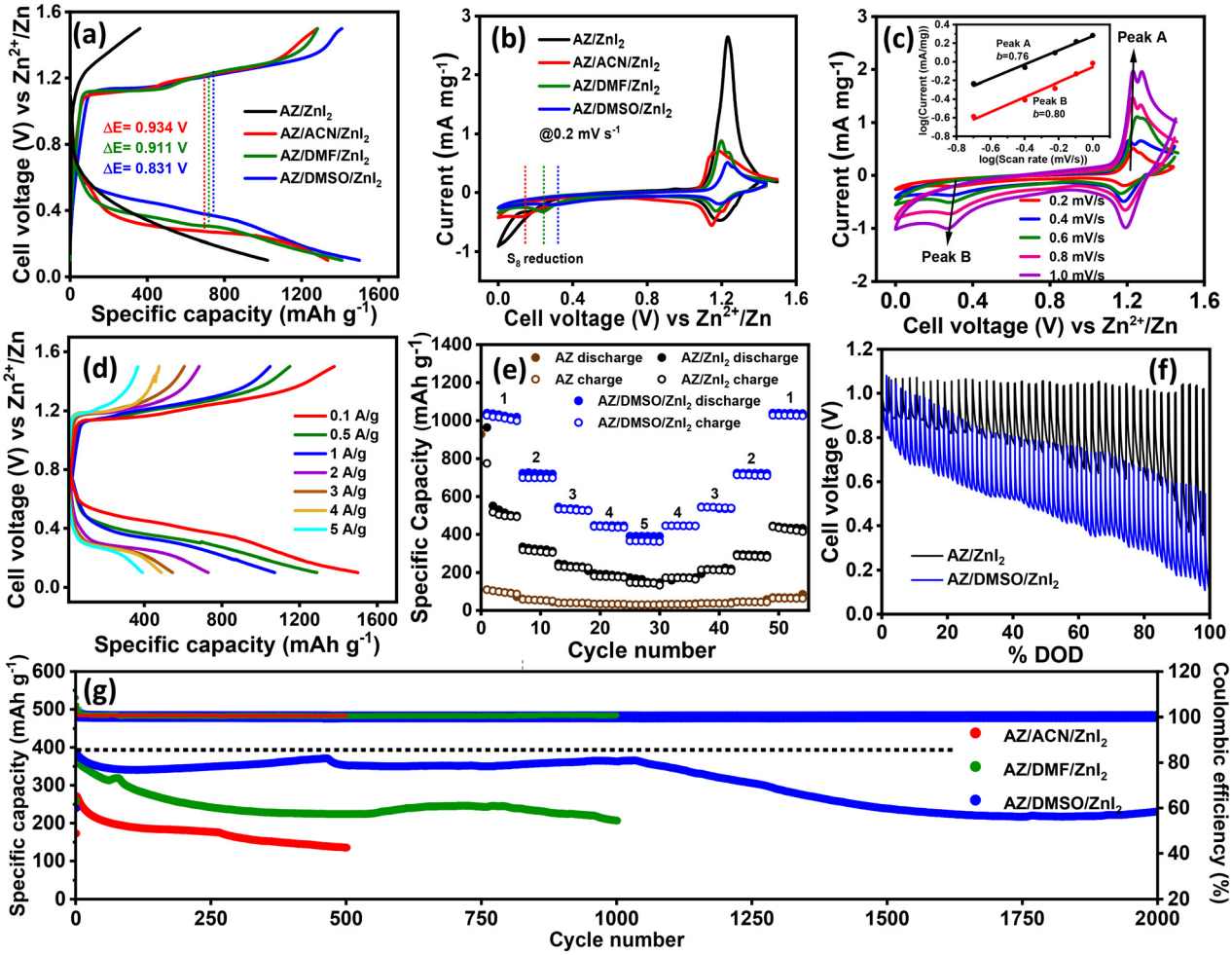

Fig. 4 (a) Specific capacity plot of full-cell Zn/S batteries using AZ/ZnI_2, AZ/ACN/ZnI_2, AZ/DMF/ZnI_2, and AZ/DMSO/ZnI_2 electrolytes at 0.1 A g^{-1} (b) CV curves of the Zn/S batteries in AZ/ZnI_2, AZ/ACN/ZnI_2, AZ/DMF/ZnI_2, and AZ/DMSO/ZnI_2 electrolytes at 0.2 mV s^{-1}; (c) CV curves of the Zn/S batteries at different scan rates in AZ/DMSO/ZnI_2; (d) GCD curves of the Zn/S battery in AZ/DMSO/ZnI_2 at different current densities; (e) rate performance of the Zn/S battery in AZ, AZ/ZnI_2 and AZ/DMSO/ZnI_2; (f) GITT profiles of the Zn/S battery in AZ/ZnI_2 and AZ/DMSO/ZnI_2; and (g) long-term cycling performance of the Zn/S batteries in AZ/ACN/ZnI_2, AZ/DMF/ZnI_2, and AZ/DMSO/ZnI_2 at 5 A g^{-1}.

with the rise in the solvent DN, leading to a reduction in overpotential (ΔE) from 0.93 V in ACN-40 to 0.91 V with DMF-40 and finally down to 0.83 V with DMSO-20. In contrast, the battery assembled with the AZ/ZnI_2 electrolyte exhibited poor performance. CV measurements at a scan rate of 0.2 mV s^{-1} (Fig. 4b) revealed well-defined redox behavior corresponding to sulfur redox reactions, featuring one cathodic and one anodic peak for all the electrolytes. The redox pairs at 0.32 V and 1.22 V for AZ/DMSO/ZnI_2 corresponded to the reduction of S_8 to ZnS and the oxidation of ZnS to S_8, respectively. A decrease in the cathodic current at 0.32 V in the AZ/DMSO/ZnI_2 hybrid electrolyte indicates enhanced stability due to DMSO, whereas the AZ/ZnI_2 electrolyte lacked a distinct sulfur reduction peak, likely due to parasitic H_2 evolution. Additionally, a redox couple at 1.18/1.27 V was attributed to iodide/iodine conversion, as confirmed by the CV recorded using an AC cathode (Fig. S6a, ESI†). AZ/ACN/ZnI_2 exhibited the sulfur reduction peak at a lower voltage (0.14 V) compared to AZ/DMSO/ZnI_2, indicating sluggish sulfur conversion kinetics in the presence of ACN. These observations corroborate the results obtained from GCD, emphasizing the role of high DN additives, particularly DMSO, in stabilizing the battery performance. To further evaluate the role of DMSO, the CV of the batteries was recorded at various scan rates ranging from 0.2 mV s^{-1} to 1 mV s^{-1}. The well-defined redox peaks with negligible changes in peak potential and shape with increasing scan rate in Fig. 4c demonstrate excellent cathode stability. The power-law equation $i = av^b$ (where i = peak current and v = scan rate) revealed the slope (b) values of 0.76 for cathodic (peak A) and 0.80 for anodic (peak B) processes, suggesting a diffusion-controlled and surface-controlled redox process in AZ/DMSO/ZnI_2.[14,41]

The charge–discharge curves in Fig. 4d show that the battery with AZ/DMSO/ZnI_2 achieved an impressive initial discharge capacity of 1502 mA h g^{-1} and an energy density of 556 W h kg^{-1} at 0.1 A g^{-1} with respect to sulfur, outperforming the

AZ and AZ/ZnI_2 systems, which delivered capacities of 1203 and 1024 mA h g^{-1} at 0.1 A g^{-1}, respectively (Fig. 4a and S6b, ESI†). Upon the addition of the organic co-solvent DMSO, the formation of $[Zn(H_2O)_m(DMSO)_n]^{2+}$ results in a lower ionic conductivity owing to increased ionic radii compared to $[Zn(H_2O)_6]^{2+}$ and thus results in slower diffusion of zinc ions in the electrolyte.[42] This leads to reduced discharge voltage for a battery containing the AZ/DMSO/ZnI_2 electrolyte. A comparison of Zn/S battery performance from the literature, as presented in Table S11 (ESI†), shows that our battery system delivers a comparable capacity. Moreover, the AZ/DMSO/ZnI_2 battery exhibited reversible high capacities of 1502, 1293, 1074, 731, 544, 484, and 386 mA h g^{-1} across current densities from 0.1 A g^{-1} to 5 A g^{-1} (Fig. 4d). To further check the stability of the battery in the hybrid electrolyte, rate performance was studied, wherein upon increasing the current density from 1 A g^{-1} to 5 A g^{-1}, the battery containing AZ/DMSO/ZnI_2 delivered a reversible capacity that decreased with increasing current density. Notably, when the current density was reverted to 1 A g^{-1}, the capacity recovered nearly to its initial value, demonstrating outstanding rate capability and stability (Fig. 4e). In contrast, AZ/ZnI_2 and AZ electrolytes exhibited lower reversibility and capacity retention.

The superior performance of AZ/DMSO/ZnI_2 was attributed to the improved electrolyte wettability of the sulfur cathode. Wettability is a crucial factor in optimizing the interaction between the cathode and the electrolyte, significantly affecting zinc ion diffusion and electrode kinetics. Water contact angle (WCA) measurements revealed a high WCA of 116.5° for the AZ/ZnI_2 electrolyte, signifying poor wettability, while AZ/ACN-40/ZnI_2, AZ/DMF-40/ZnI_2, and AZ/DMSO-20/ZnI_2 electrolytes exhibited markedly lower WCAs of 33.7°, 35.9°, and 35.1°, respectively (Fig. S7, ESI†). Notably, enhanced wettability was also observed when sulfur powder was soaked in ACN–water, DMF–water, and DMSO–water solutions compared to water alone, consistent with the measured WCA values (Fig. S8, ESI†). Organic co-solvents as additives reduce the surface energy and enhance electrolyte penetration into the sulfur cathode matrix, thereby improving Zn ion diffusion and facilitating charge transfer efficiency during cycling.

Enhanced Zn ion diffusion in the presence of DMSO is associated with accelerated redox kinetics at the electrode/electrolyte interface, as evidenced by EIS and galvanostatic intermittent titration technique (GITT) measurements. The GITT measurements used to examine ion diffusion revealed that the diffusion coefficient in the battery utilizing AZ/DMSO/ZnI_2 falls in the range of 10^{-16} to 10^{-15} cm^2 s^{-1}, which is nearly an order of magnitude higher than that of the AZ/ZnI_2 (ranging between 10^{-18} and 10^{-16} cm^2 s^{-1}) (Fig. 4f and S9, ESI†). A higher *iR* drop at the late discharge state is observed in the battery using AZ/ZnI_2 due to the increase in concentration polarization.[43] The Nyquist plot from the EIS analysis in Fig. S10 (ESI†) confirmed a lower charge transfer resistance (R_{ct}) in hybrid electrolytes, suggesting improved ion diffusion in the presence of DMSO. Additionally, the exchange current density (j_0) was calculated to understand the redox kinetics (detailed in the ESI†), wherein j_0 for AZ/DMSO/ZnI_2 was found to be 10.95×10^{-2} mA cm^{-2}, 2.5-fold higher than that of AZ/ZnI_2 (4.46×10^{-2} mA cm^{-2}). For comparison, j_0 was calculated for AZ/ACN/ZnI_2 and AZ/DMF/ZnI_2, among which DMSO exhibited the highest j_0, demonstrating that DMSO facilitates better zinc diffusion into the sulfur cathode (Table S10, ESI†). Long-term cycling stability analysis in Fig. 4g revealed that the AZ/DMSO/ZnI_2 battery maintained improved long-term stability at a high current density of 5 A g^{-1}, with a capacity retention of 92% after 1000 cycles and 62% after 2000 cycles. In contrast, AZ/ACN/ZnI_2 and AZ/DMF/ZnI_2 retained only 50% and 55% of their initial capacity after 500 cycles and 1000 cycles, respectively, highlighting the pivotal role of DMSO as an additive in enhancing battery performance.

Furthermore, XPS and Raman analyses were performed on the retrieved cathodes at various charge–discharge potentials to elucidate the sulfur conversion mechanism. As shown in Fig. 5a, prior to discharge (Point A), peaks corresponding to sulfur (S_8), S=O (DMSO) at 166.9 eV and 168.21 eV, and $CF_3SO_3^-$ at 168.9 eV and 170.2 eV were observed. Upon discharging to 0.35 V (Point B), the S_8 peak decreased, and a ZnS peak began to emerge. When the battery was further discharged to 0.1 V (Point C), the ZnS peak became predominant, with only minimal residual sulfur detected. During the reverse process, charging the battery to 1.35 V (Point D) resulted in the reappearance of the sulfur peak, while the ZnS peak completely disappeared upon charging to 1.5 V (Point E). Similarly, the peaks at 148, 220, and 472 cm^{-1} in Raman spectra corresponding to S_8 gradually diminished when discharged, while peaks at 186, 330, 372, and 405 cm^{-1} for ZnS became dominant (Fig. 5b). Upon subsequent charging, the peaks for S_8 re-emerged with the disappearance of ZnS, implying a direct solid–solid conversion between sulfur and ZnS. FESEM and EDAX analysis of the retrieved sulfur electrodes at different cycling stages indicated a progressive accumulation of dead active material on the carbon surface, which reduces its participation in the successive cycling process, contributing to the observed capacity degradation to 62% after 2000 cycles (Fig. 5d–f, and S11, ESI†). Furthermore, to explore the effective utilization of AZ/DMSO/ZnI_2, two Zn/S batteries were assembled in series, providing an open-circuit potential (OCP) of 2.12 V, which successfully powered a 1.8 V red LED, demonstrating the practical utility of the designed battery (Fig. 5c and S12, ESI†).

2.5 Role of the DMSO-based hybrid electrolyte in suppressing parasitic reactions at the Zn anode

The zinc metal anode is plagued by dendritic growth and passivation during electrochemical cycling, leading to suboptimal zinc utilization and reduced efficiency. To evaluate the efficacy of the hybrid electrolyte in mitigating dendritic growth and parasitic reactions at the anode, Zn||Zn symmetric cells were assembled using both aqueous and hybrid electrolytes. Voltage hysteresis and morphological changes in the zinc anode during stripping/plating were analyzed at a current density of 2 mA cm^{-2} and an areal capacity of 1 mA h cm^{-2}.

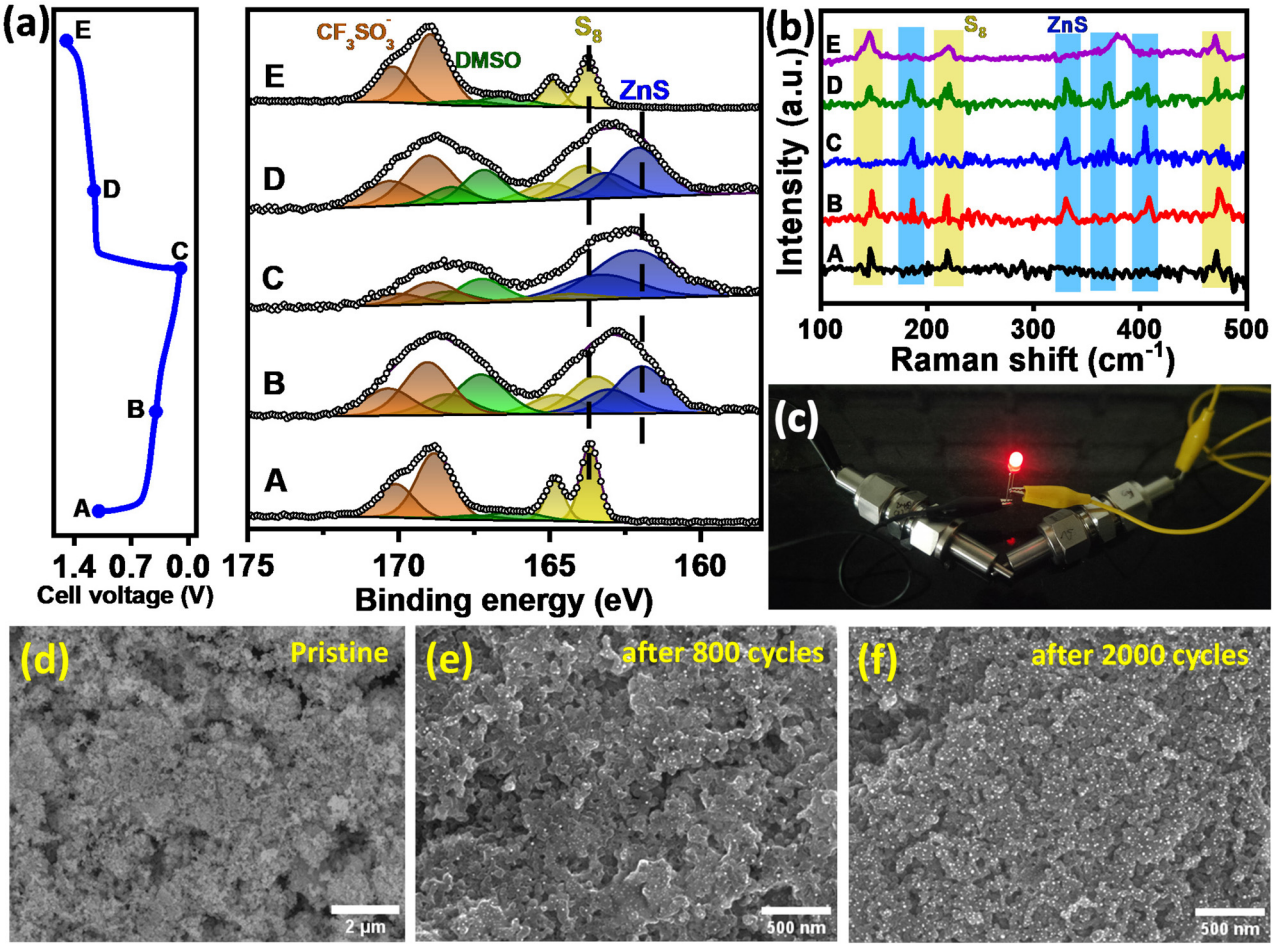

Fig. 5 (a) XPS and (b) Raman spectra of S@AC at different charge–discharge voltages; (c) photograph of an LED powered by assembling two Zn/S batteries using the AZ/DMSO/ZnI_2 electrolyte; FESEM images of the sulfur cathode: (d) pristine, (e) after 800 cycles, and (f) after 2000 cycles.

The Zn||Zn symmetric cell with the AZ/DMSO/ZnI_2 electrolyte demonstrated excellent cycling stability with a flat voltage profile, maintaining performance for 500 h (tested up to 500 h only). In stark contrast, the cell with the aqueous electrolyte (AZ/ZnI_2) showed voltage fluctuations due to the large polarization resistance resulting from the dendritic Zn growth and failed abruptly after a cycling life of 44 hours (Fig. 6a). This confirms that the DMSO-containing hybrid electrolyte promotes a stable voltage profile and ensures a highly reversible Zn plating/stripping process. Furthermore, EIS recorded at the 10^{th} cycle and the final cycle revealed a decrease in charge transfer resistance (R_{ct}) during cycling, implying the formation of a stable and integrated electrode/electrolyte interface. In contrast, an increase in R_{ct} was observed for the aqueous electrolyte over time, underscoring the positive effect of DMSO in stabilizing the electrode/electrolyte interface, thereby enhancing the lifecycle of the AZ/DMSO/ZnI_2 operated Zn||Zn cell (Fig. 6b and c). DFT calculations provided additional insights, showing that increasing DMSO content lowers the LUMO energy level to a great extent, thereby improving the efficiency of accepting electrons by Zn^{2+} during plating on the Zn anode. The LUMO energy decreased from −0.56 eV for $[Zn(H_2O)_6]^{2+}$ to −1.05 eV for $[Zn(H_2O)_6(DMSO)_1]^{2+}$ and −1.25 eV for $[Zn(H_2O)_4(DMSO)_2]^{2+}$, explaining the much reduced hysteresis in the presence of DMSO (Fig. S13, ESI†).

Post-cycling morphological changes and Zn anode composition were evaluated using optical images, FESEM, and PXRD to understand the surface and nature of products formed during cycling. Optical images revealed a smooth surface for the Zn anode cycled in AZ/DMSO/ZnI_2, indicating suppression of dendritic growth and effective corrosion mitigation. In contrast, the Zn anode cycled in AZ/ZnI_2 exhibited a rough, non-uniform surface (Fig. 6d and e). *Ex situ* FESEM analysis provided more detailed insights into the surface morphology. Significant cracking and flake-like Zn protuberances were observed, indicating severe dendritic growth on the Zn anode in AZ/ZnI_2 (Fig. 6f). In stark contrast, Zn anodes cycled in AZ/DMSO/ZnI_2 exhibited a smoother morphology even after 500 hours, indicating uniform Zn deposition during stripping/plating (Fig. 6g). This suggests that DMSO facilitates homogeneous nucleation, preventing the formation of corrosion products and "dead" Zn, thereby enhancing anode stability during long-term cycling.

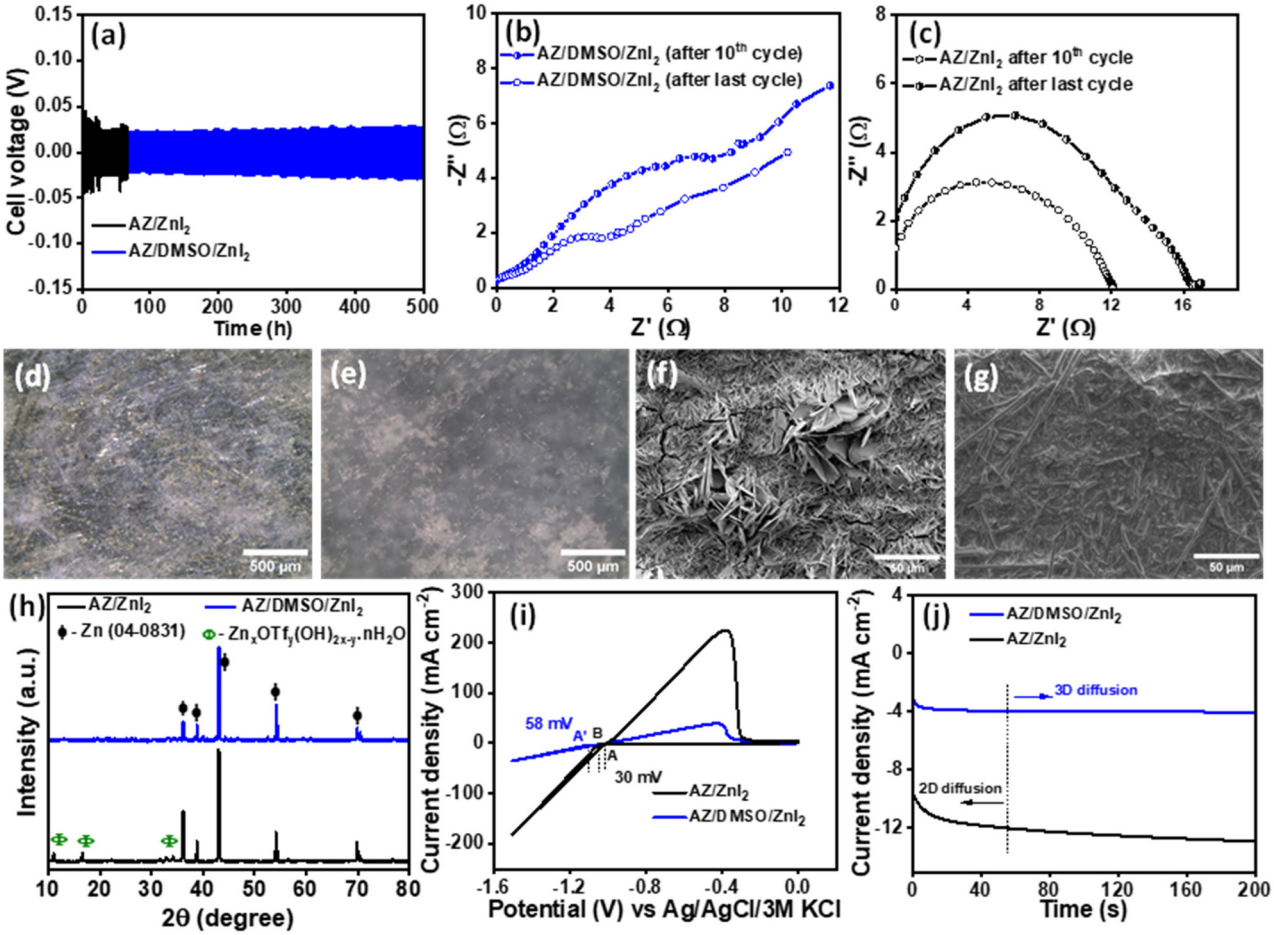

Fig. 6 (a) Zn stripping/plating of Zn||Zn symmetric cells in AZ/ZnI_2 and $AZ/DMSO/ZnI_2$ electrolytes at 2 mA cm^{-2} and 1 mA h cm^{-2}; EIS spectra of Zn||Zn symmetric cells (after the 10^{th} cycle and the last cycle at 2 mA cm^{-2}) in (b) $AZ/DMSO/ZnI_2$ and (c) AZ/ZnI_2; optical images of Zn after Zn||Zn symmetric cell cycling in (d) AZ/ZnI_2 and (e) $AZ/DMSO/ZnI_2$, and corresponding *ex situ* FESEM in (f) AZ/ZnI_2 and (g) $AZ/DMSO/ZnI_2$ electrolytes; (h) PXRD spectra of zinc electrodes after cycling; (i) nucleation overpotential for Zn nucleation from CV at a scan rate of 20 mV s^{-1} using graphite, Ag/AgCl/3 M KCl, and Zn as the working, reference, and counter electrodes, respectively; and (j) chronoamperometry of the Zn||Zn symmetric cell in AZ/ZnI_2 and $AZ/DMSO/ZnI_2$ electrolytes.

Uneven Zn deposition and formation of corrosion products in AZ/ZnI_2 were studied using post-cycling PXRD analysis, wherein characteristic peaks of corrosion products like $Zn_xOTf_y(-OH)_{2x-y}{\cdot}nH_2O$ were observed (Fig. 6h).[20] In stark contrast, the Zn anode cycled in $AZ/DMSO/ZnI_2$ exhibited characteristic Zn peaks at 36° and 43° (PDF#04-0831), suggesting an efficient suppression of corrosive products by DMSO, causing uniform Zn deposition during the stripping/plating process. The nucleation and deposition kinetics of Zn^{2+} ions are crucial in determining the battery cycling stability. Dendritic growth often occurs due to uneven Zn deposition caused by the "tip effect" that can arise from poor nucleation control. To study Zn nucleation behaviour in different electrolytes, cyclic voltammograms (CV) were recorded using a graphite sheet, Ag/AgCl/3 M KCl, and Zn as the working, reference, and counter electrodes, respectively, at 20 mV s^{-1}. As shown in Fig. 6i, a nucleation overpotential (NOP) of 58 mV (A–A′) was obtained for $AZ/DMSO/ZnI_2$, which is higher than those of AZ/ZnI_2 electrolytes having an NOP value of 30 mV (A–B) owing to the higher desolvation energy associated with DMSO. It is well known that a higher NOP leads to a smaller nucleation radius and a strong driving force for nucleation, which promotes finer and more uniform Zn deposition. Thus, the higher NOP observed for the DMSO-containing hybrid electrolyte facilitates the formation of fine-grained Zn deposition. In contrast, the lower NOP for AZ/ZnI_2 leads to faster and uneven Zn deposition and dendritic growth, as evidenced by FESEM analysis.[44] To gain deeper insights into Zn deposition behaviour, chronoamperometry (CA) of the Zn||Zn symmetric cell was performed at a constant voltage of −0.15 V for 120 seconds. The increasing current density in AZ/ZnI_2 over time implied 2D diffusion and uneven deposition. Conversely, the current density in $AZ/DMSO/ZnI_2$ stabilized within 15 s through a 3D diffusion process, which promotes compact and uniform Zn deposition, as seen in Fig. 6j.[36] The excellent performance of the hybrid electrolyte in mitigating corrosion and dendritic growth of the Zn anode was

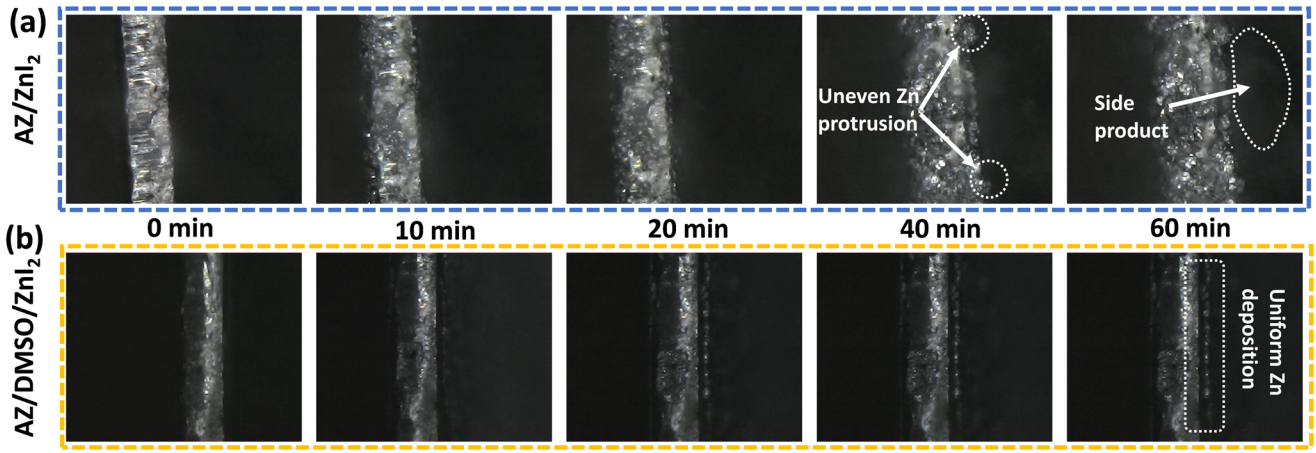

Fig. 7 *In situ* optical microscopic observation of Zn deposition in (a) AZ/ZnI_2 and (b) $AZ/DMSO/ZnI_2$ electrolytes after various deposition times at 10 mA cm^{-2}.

further examined using *in situ* optical microscopy at various deposition times at 10 mA cm^{-2}. As shown in Fig. 7a, uneven Zn protrusions began to emerge on the surface after 10 minutes, gradually developing into dendrites and the surface was covered with side products within 60 minutes of deposition time. In contrast, DMSO-containing hybrid electrolytes led to uniform Zn deposition (Fig. 7b). The optical microscopic images of the Zn post-deposition show that AZ/ZnI_2 electrolytes caused uneven zinc plating, while the $AZ/DMSO/ZnI_2$ hybrid electrolyte demonstrated a homogeneous and even surface (Fig. S14a and b, ESI†). The above studies present high-donor number solvents like DMSO as an effective strategy to regulate the solvation sheath of Zn^{2+} ions and enhance anode stabilization and sulfur conversion kinetics to deliver high-capacity Zn/S batteries.

3 Conclusion

In summary, we have utilized the electrolyte engineering strategy by exploiting a high-donor number solvent additive DMSO for enhancing the performance of high energy-dense rechargeable Zn/S batteries. Spectroscopic and electrochemical analyses revealed that DMSO-based hybrid electrolytes serve a dual function: (i) facilitating zinc ion mobility at the electrode/electrolyte interface and reducing water activity, which enables uniform zinc plating and mitigates dendrite formation and (ii) enhancing sulfur cathode wettability and utilization, leading to superior cycling stability. Zn||Zn symmetric cells with DMSO-containing electrolytes exhibited uniform zinc deposition over 500 hours and five-fold lower corrosion compared to aqueous electrolytes. Zn/S batteries utilizing $AZ/DMSO/ZnI_2$ delivered an impressive initial capacity of 1502 mA h g^{-1} at 0.1 A g^{-1} and a high energy density of 556 W h kg^{-1}. Remarkably, these batteries retained 92% capacity after 1000 cycles and 62% after 2000 cycles at a high current density of 5 A g^{-1}, demonstrating exceptional cycling stability. Furthermore, high-DN DMSO as an additive effectively minimized zinc corrosion and the HER even at lower concentrations compared to higher concentrations of low-DN solvents. Finally, the practical viability of the Zn/S battery was demonstrated by successfully powering an LED, underscoring the potential of high-DN solvents to stabilize the cathode/electrolyte interface and develop cost-effective, high-performance, and safer aqueous Zn/S batteries.

Data availability

The data supporting this article have been included as part of the ESI.†

Conflicts of interest

The authors declare no competing financial interests.

Acknowledgements

D. Mandal acknowledges SERB (CRG/2023/004666) and CSIR (02(0436/21/EMR-II)) for financial support. Tino S. Thomas (DEC18-114672) thanks UGC for the fellowship, and Aayushi P. Sinha thanks DST for the Inspire Fellowship (DST/INSPIRE/03/2019/000968). The authors thank the CRF facility, IIT Ropar, for XPS, Raman, and FESEM analysis.

References

1 A. Gupta, A. Bhargav and A. Manthiram, *ACS Energy Lett.*, 2021, **6**, 224–231.
2 A. Manthiram, *Nat. Commun.*, 2020, **11**, 1550.
3 C. P. Grey and D. S. Hall, *Nat. Commun.*, 2020, **11**, 6279.

4 P. G. Bruce, S. A. Freunberger, L. J. Hardwick and J.-M. Tarascon, *Nat. Mater.*, 2012, **11**, 19–29.
5 X. Ji and L. F. Nazar, *J. Mater. Chem.*, 2010, **20**, 9821–9826.
6 X. Ji, K. T. Lee and L. F. Nazar, *Nat. Mater.*, 2009, **8**, 500–506.
7 S. S. Zhang and J. A. Read, *J. Power Sources*, 2012, **200**, 77–82.
8 M. Luo, C. Wang, H. Lu, Y. Lu, B. B. Xu, W. Sun, H. Pan, M. Yan and Y. Jiang, *Energy Storage Mater.*, 2021, **41**, 515–521.
9 J. Yang, Y. Zhang, Z. Li, X. Xu, X. Su, J. Lai, Y. Liu, K. Ding, L. Chen, Y.-P. Cai and Q. Zheng, *Adv. Funct. Mater.*, 2022, **32**, 2209642.
10 C. Wei, Y. Wang, Z. Ding, T. Fang, J. Song, Y. Zhang, S. Lv, X. Liu and X. Tang, *Adv. Funct. Mater.*, 2023, **33**, 2212644.
11 Y. Guo, X. Zhu, J. Zhang, T. Zhang, Z. Wang, M. Shan, F. Wang, C. C. Cao, G. Xu and M. Zhu, *Angew. Chem.*, 2024, **64**, e202422047.
12 T. S. Thomas, A. P. Sinha and D. Mandal, *J. Mater. Chem. A*, 2024, **12**, 21350–21356.
13 H. Zhang, Z. Shang, G. Luo, S. Jiao, R. Cao, Q. Chen and K. Lu, *ACS Nano*, 2022, **16**, 7344–7351.
14 M. Yang, Z. Yan, J. Xiao, W. Xin, L. Zhang, H. Peng, Y. Geng, J. Li, Y. Wang, L. Liu and Z. Zhu, *Angew. Chem., Int. Ed.*, 2022, **61**, e202212666.
15 H. Shahali, R. Sellers, A. Rafieerad, A. A. Polycarpou and A. Amiri, *Energy Storage Mater.*, 2024, **65**, 103130.
16 P. Hei, Y. Sai, C. Liu, W. Li, J. Wang, X. Sun, Y. Song and X.-X. Liu, *Angew. Chem., Int. Ed.*, 2024, **63**, e202316082.
17 M. Li, Z. Li, X. Wang, J. Meng, X. Liu, B. Wu, C. Han and L. Mai, *Energy Environ. Sci.*, 2021, **14**, 3796–3839.
18 S. Chen, D. Ji, Q. Chen, J. Ma, S. Hou and J. Zhang, *Nat. Commun.*, 2023, **14**, 3526.
19 Y. Yang, C. Liu, Z. Lv, H. Yang, X. Cheng, S. Zhang, M. Ye, Y. Zhang, L. Chen, J. Zhao and C. C. Li, *Energy Storage Mater.*, 2021, **41**, 230–239.
20 Y. Guo, R. Chua, Y. Chen, Y. Cai, E. J. J. Tang, J. J. N. Lim, T. H. Tran, V. Verma, M. W. Wong and M. Srinivasan, *Small*, 2023, **19**, 2207133.
21 Y. Zhang, A. Amardeep, Z. Wu, L. Tao, J. Xu, D. J. Freschi and J. Liu, *Adv. Sci.*, 2024, **11**, 2308580.
22 G. Chang, J. Liu, Y. Hao, C. Huang, Y. Yang, Y. Qian, X. Chen, Q. Tang and A. Hu, *Chem. Eng. J.*, 2023, **457**, 141083.
23 W. Zhang, M. Wang, J. Ma, H. Zhang, L. Fu, B. Song, S. Lu and K. Lu, *Adv. Funct. Mater.*, 2023, **33**, 2210899.
24 S. Wang, W. Wu, Q. Jiang, C. Li, H.-Y. Shi, X.-X. Liu and X. Sun, *Chem. Sci.*, 2025, **16**, 1802–1808.
25 W. Wu, S. Wang, L. Lin, H.-Y. Shi and X. Sun, *Energy Environ. Sci.*, 2023, **16**, 4326–4333.
26 F. Zhang, Q. Meng, J.-W. Qian, J. Chen, W.-X. Dong, K. Chen, Y.-F. Cui, S. X. Dou and L.-F. Chen, *Angew. Chem., Int. Ed.*, 2025, e202425487.
27 F. Zhang, J.-W. Qian, W.-X. Dong, Y.-F. Qu, K. Chen, J. Chen, Y.-F. Cui and L.-F. Chen, *Energy Environ. Sci.*, 2024, **17**, 7258–7270.
28 Y.-F. Qu, X. Liu, J.-W. Qian, J. Chen and L.-F. Chen, *Batteries Supercaps*, 2024, **7**, e202400159.
29 Y.-F. Qu, J.-W. Qian, F. Zhang, Z. Zhu, Y. Zhu, Z. Hou, Q. Meng, K. Chen, S. X. Dou and L.-F. Chen, *Adv. Mater.*, 2025, **37**, 2413370.
30 W. Deng, Z. Xu and X. Wang, *Energy Storage Mater.*, 2022, **52**, 52–60.
31 Y. Gong, R. Lin, B. Wang, H. Ren, L. Wang, H. Zhang, J. Wang, D. Li, Y. Xiong, D. Wang, H. Liu and S. Dou, *J. Energy Chem.*, 2024, **95**, 626–635.
32 V. Gutmann, *Electrochim. Acta*, 1976, **21**, 661–670.
33 W. Kao-ian, M. T. Nguyen, T. Yonezawa, R. Pornprasertsuk, J. Qin, S. Siwamogsatham and S. Kheawhom, *Mater. Today Energy*, 2021, **21**, 100738.
34 L. Cao, D. Li, E. Hu, J. Xu, T. Deng, L. Ma, Y. Wang, X.-Q. Yang and C. Wang, *J. Am. Chem. Soc.*, 2020, **142**, 21404–21409.
35 H. Ren, S. Li, L. Xu, L. Wang, X. Liu, L. Wang, Y. Liu, L. Zhang, H. Zhang, Y. Gong, C. Lv, D. Chen, J. Wang, Q. Lv, Y. Li, H. Liu, D. Wang, T. Cheng, B. Wang, D. Chao and S. Dou, *Angew. Chem., Int. Ed.*, 2025, e202423302.
36 J. Luo, L. Xu, Y. Zhou, T. Yan, Y. Shao, D. Yang, L. Zhang, Z. Xia, T. Wang, L. Zhang, T. Cheng and Y. Shao, *Angew. Chem., Int. Ed.*, 2023, **62**, e202302302.
37 M. Baek, H. Shin, K. Char and J. W. Choi, *Adv. Mater.*, 2020, **32**, 2005022.
38 Q. Zou, Y. Sun, Z. Liang, W. Wang and Y.-C. Lu, *Adv. Energy Mater.*, 2021, **11**, 2101552.
39 F. Ming, Y. Zhu, G. Huang, A.-H. Emwas, H. Liang, Y. Cui and H. N. Alshareef, *J. Am. Chem. Soc.*, 2022, **144**, 7160–7170.
40 X. Shi, J. Zeng, A. Yi, F. Wang, X. Liu and X. Lu, *J. Am. Chem. Soc.*, 2024, **146**, 20508–20517.
41 J. Wang, J. Polleux, J. Lim and B. Dunn, *J. Phys. Chem. C*, 2007, **111**, 14925–14931.
42 D. Feng, F. Cao, L. Hou, T. Li, Y. Jiao and P. Wu, *Small*, 2021, **17**, 2103195.
43 C. Yang, L. Suo, O. Borodin, F. Wang, W. Sun, T. Gao, X. Fan, S. Hou, Z. Ma, K. Amine, K. Xu and C. Wang, *Proc. Natl. Acad. Sci. U. S. A.*, 2017, **114**, 6197–6202.
44 C. Li, H. Wang, S. Chen, Z. Bai, M. Zhu, H. Wang, D. Chen, Z. Ren, S. Chen, Y. Tang and Y. Zhang, *Small*, 2024, **20**, 2306939.